

A Direct Flux Reconstruction Scheme for Advection–Diffusion Problems on Triangular Grids

J. Romero¹ · F. D. Witherden¹ · A. Jameson¹

Received: 31 January 2017 / Revised: 22 May 2017 / Accepted: 25 May 2017
© Springer Science+Business Media New York 2017

Abstract The direct flux reconstruction (DFR) scheme is a high-order numerical method which is an alternative realization of the flux reconstruction (FR) approach. In 1D, the DFR scheme has been shown to be equivalent to the FR variant of the nodal discontinuous Galerkin scheme. In this article, the DFR approach is extended to triangular elements for advection and advection–diffusion problems. This was accomplished by combining aspects of the SD–RT variant of the spectral difference (SD) scheme for triangles, with modifications motivated by characteristics of the DFR scheme in one dimension. Von Neumann analysis is applied to the new scheme and linear stability is found to be dependent on the location of internal collocation points. This is in contrast to the standard FR scheme. This analysis indicates certain internal point sets can result in schemes which exhibit weak stability; however, stable and accurate solutions to a number of linear and nonlinear benchmark problems are readily obtained.

Keywords High order methods · Flux reconstruction · Spectral difference · Triangular elements · Compressible navier–stokes

1 Introduction

In recent years, there has been an increased interest in using high-order numerical methods for conducting scale-resolving simulations of unsteady flows. The promise of these methods is increased solution accuracy using fewer total degrees of freedom. Recently, CFD codes utilizing high-order numerical methods have been successful in producing high-fidelity solutions to challenging flow problems at scale on modern computing hardware [32]. As such, these methods have become increasingly competitive, relative to industry-standard tools

Dedicated to Professor Chi-Wang Shu on the occasion of his 60th birthday

✉ J. Romero
jdromero@stanford.edu

¹ Department of Aeronautics and Astronautics, Stanford University, Stanford, CA 94305, USA

based around second-order formulations [31]. A popular class of high-order methods that are particularly suitable for solving the compressible Navier–Stokes equations are those based around the flux reconstruction (FR) approach of Huynh [16]. The FR method is based on the differential form of the governing equations and has been shown to recover other popular high-order schemes [2, 14, 24, 25], such as a nodal discontinuous Galerkin (DG) scheme similar to that described by Hesthaven and Warburton [15], and the spectral difference (SD) scheme, which was originally developed by Kopriva and Kolias [21]. These schemes are all offshoots of the classical discontinuous Galerkin (DG) scheme, developed by Cockburn and Shu for conservation laws in a seminal series of papers [7–10, 12]. In 2009, Huynh developed an extension of the FR method for advection–diffusion problems [17]. By extension of a proof of linear stability for the SD method developed by Jameson [18], Vincent et al. [34] identified a family of provably linearly stable FR schemes for advection problems, known as the energy stable flux reconstruction (ESFR) schemes. These schemes were later extended to advection–diffusion problems by Castonguay et al. [5]. More recently, Romero et al. developed the direct flux reconstruction (DFR) scheme, a simplified formulation of the FR scheme which does not utilize correction functions [28]. Using a tensor-product formulation described by Huynh [16], the FR and DFR schemes in 1D can be easily extended to problems in 2D using quadrilateral elements and 3D using hexahedral elements.

To increase the utility of these schemes for simulating flows over complex geometrical configurations, much effort has been made to develop extensions to triangular and tetrahedral elements. Castonguay et al. developed a formulation of the ESFR schemes for advection on triangles [4] which was later extended to advection–diffusion problems on triangles and tetrahedra by Williams et al. [35, 37]. Furthermore, a generalized formulation of the SD scheme on triangles was developed by Liu et al. [22]. A variation of the SD scheme on triangles for convective problems, using a flux interpolation procedure spanning a Raviart–Thomas basis [27], known as the SD–RT scheme was developed by May et al. [23] and extended to the Euler equations by Balan et al. [3].

In this paper, an extension of the DFR scheme to advection–diffusion problems on triangular elements is presented. The newly developed scheme maintains many of the defining characteristics of the existing DFR scheme for one-dimensional problems, in particular, a flux divergence computation of one degree higher than that of the solution and an absence of the use of correction functions. The paper begins with a review of the existing one-dimensional formulation of the DFR scheme for advection–diffusion problems. This review is followed by the development of the DFR scheme for advection–diffusion problems on triangular elements. As part of this development, we introduce a new approach to computing the solution gradients required by the diffusive flux term. Next, von Neumann analysis of a simple linear advection problem is carried out to analyze the linear stability properties of the scheme. Finally, several test cases, both linear and non-linear, are conducted to assess the accuracy and numerical performance of the new scheme in different contexts, followed by concluding remarks.

2 Review of DFR in 1D

In order to motivate the development of the DFR formulation on triangles, a brief review of the existing DFR scheme and its defining features in one dimension is provided.

2.1 Preliminaries

Consider a 1D scalar conservation law

$$\frac{\partial u}{\partial t} + \frac{\partial f}{\partial x} = 0, \quad (1)$$

defined within a one-dimensional domain $\Omega \in \mathbb{R}$ where x is the spatial coordinate, t is time, $u = u(x, t)$ is a scalar quantity and $f = f(u, \frac{\partial u}{\partial x})$ is a flux function which depends on the scalar and its derivative. For advection–diffusion, the flux can be split as $f = f_{adv} + f_{dif}$, with $f_{adv} = f_{adv}(u)$ corresponding to the convective flux which depends only on the scalar u , and $f_{dif} = f_{dif}(u, \frac{\partial u}{\partial x})$ corresponding to the diffusive flux which depends on the scalar and its derivative. Equation (1) can be split into a system of first-order equations as

$$\frac{\partial u}{\partial t} + \frac{\partial f(u, q)}{\partial x} = 0, \quad (2)$$

$$q - \frac{\partial u}{\partial x} = 0, \quad (3)$$

with the introduction of a new variable, q , which is referred to as the auxiliary variable.

Next, consider partitioning the domain Ω into N non-overlapping elements, such that $\Omega = \bigcup_{n=1}^N \Omega_n$, with each element defined as $\Omega_n = \{x | x_n \leq x < x_{n+1}\}$. Define an approximate element local system

$$\frac{\partial u_n}{\partial t} + \frac{\partial f_n}{\partial x} = 0, \quad (4)$$

$$q_n - \frac{\partial u_n^C}{\partial x} = 0, \quad (5)$$

where $u_n = u_n(x, t)$, $f_n = f_n(x, t)$, $q_n = q_n(x, t)$, and $u_n^C = u_n^C(x, t)$ are piecewise polynomial functions defined within Ω_n , taking the value of zero elsewhere in the domain Ω . The global approximations to solution u and flux f are defined as

$$u \approx \sum_{n=1}^N u_n, \quad f \approx \sum_{n=1}^N f_n. \quad (6)$$

As a requirement for conservation, f must be at least C^0 -continuous at element boundaries. The approximate solution u is allowed to be discontinuous at element boundaries; however, to facilitate the computation of q_n , an additional global quantity $u^C = \sum_{n=1}^N u_n^C$, which is referred as the *continuous* solution, is introduced that maintains at least C^0 -continuity at element boundaries.

To simplify the formulation, the elements Ω_n are each transformed to standard reference elements $\tilde{\Omega}_n = \{r | -1 \leq r \leq 1\}$ via an isoparametric mapping function $x = \theta_n(r)$ with associated geometric Jacobian, $J_n = \frac{\partial \theta_n}{\partial r}$ where r is the reference coordinate. Applying this mapping to Eqs. (4) and (5) yields a transformed system within each $\tilde{\Omega}_n$

$$\frac{\partial \tilde{u}_n}{\partial t} + \frac{1}{J_n} \frac{\partial \tilde{f}_n}{\partial r} = 0, \quad (7)$$

$$\tilde{q}_n - \frac{1}{J_n} \frac{\partial \tilde{u}_n^C}{\partial r} = 0, \quad (8)$$

where

$$\tilde{u}_n = \tilde{u}_n(r, t) = u_n(\theta_n(r), t), \quad (9)$$

$$\tilde{f}_n = \tilde{f}_n(r, t) = f_n(\theta_n(r), t), \quad (10)$$

$$\tilde{q}_n = \tilde{q}_n(r, t) = q_n(\theta_n(r), t), \quad (11)$$

$$\tilde{u}_n^C = \tilde{u}_n^C(r, t) = u_n^C(\theta_n(r), t). \quad (12)$$

2.2 Procedure for First-Order Flux

To begin, define a set of $P + 1$ *solution* points $\{r_1, r_2, \dots, r_{P+1}\}$ in the interior of the standard element. Next, define a set of $P + 3$ *flux* points $\{r_0, r_1, r_2, r_3, \dots, r_{P+1}, r_{P+2}\}$ which includes the previously defined solution points as well as additional points on the element boundaries, $r_0 = -1$ and $r_{P+2} = 1$. The number of solution points and number of flux points support polynomial interpolation of degree P and $P + 2$ respectively. Typically, the solution point locations are collocated with the zeros of the Legendre polynomial of degree $P + 1$, also referred to as the Gauss–quadrature points. This choice of solution points was shown by Romero et al. to recover the nodal DG variant of the standard FR scheme [28]. Note that by definition, the interior flux points and the solution points are coincident.

The functions \tilde{u}_n , \tilde{q}_n , and \tilde{f}_n are represented using Lagrange interpolating polynomials as

$$\tilde{u}_n = \sum_{j=1}^{P+1} u_{n,j} \ell_j, \quad (13)$$

$$\tilde{q}_n = \sum_{j=1}^{P+1} q_{n,j} \ell_j, \quad (14)$$

$$\tilde{f}_n = f_{n,0}^I \tilde{\ell}_0 + \sum_{j=1}^{P+1} f_{n,j} \tilde{\ell}_j + f_{n,P+2}^I \tilde{\ell}_{P+2}, \quad (15)$$

where $u_{n,j}$ and $q_{n,j}$ are the solution and auxiliary variable values sampled at the solution point r_j , $f_{n,j} = f_{adv}(u_{n,j}) + f_{dif}(u_{n,j}, q_{n,j})$ are the flux values computed at the solution point r_j , and $f_{n,0}^I$ and $f_{n,P+2}^I$ are imposed common interface flux values at the left and right element boundary flux points respectively. ℓ_j are Lagrange basis polynomials of degree P defined using the solution points and $\tilde{\ell}_j$ are Lagrange basis polynomials of degree $P + 2$ defined using the flux points such that

$$\ell_j(r_i) = \delta_{i,j} \quad \text{for } i, j = 1, 2, \dots, P + 1, \quad (16)$$

$$\tilde{\ell}_j(r_i) = \delta_{i,j} \quad \text{for } i, j = 0, 1, \dots, P + 2, \quad (17)$$

where $\delta_{i,j}$ is the Kronecker delta function which takes the value of one if $i = j$ and zero otherwise. The procedure to compute the auxiliary variable values $q_{n,j}$ to complete the definition of Eq. (14) will be discussed in the subsequent section.

The common interface flux values $f_{n,j}^I$ are imposed at the boundary flux points in Eq. (15) to meet continuity requirements of the flux function for conservation. The common interface flux values can be split into two components

$$f_{n,j}^I = F_{adv}(u_L, u_R) + F_{dif}(u_L, u_R, q_L, q_R), \quad (18)$$

where the subscripts \square_L and \square_R refer to values at the flux point computed using information from the left and right elements at the boundary respectively, and $F_{adv}(u_L, u_R)$ and $F_{dif}(u_L, u_R, q_L, q_R)$ are common flux functions associated with the advective and diffusive fluxes respectively. A typical choice for F_{adv} is the Rusanov flux function [29], which is also

referred to as the Lax–Friedrichs flux [15] for linear fluxes, and a typical choice for F_{dif} is the local discontinuous Galerkin (LDG) [11] flux function.

With the common flux values defined, substitution of Eq. (15) into Eq. (7) yields the following semi-discrete equation for the DFR scheme

$$\frac{d\tilde{u}_n}{dt} + \frac{1}{J_n} \left[f_{n,0}^I \frac{d\bar{\ell}_0}{dr} + \sum_{j=1}^{P+1} f_{n,j} \frac{d\bar{\ell}_j}{dr} + f_{n,P+2}^I \frac{d\bar{\ell}_{P+2}}{dr} \right] = 0. \quad (19)$$

Equation (19) describes a system of ordinary differential equations in t which can be marched forward in time using a number of time integration schemes, for example, the classical fourth order Runge–Kutta (RK4) scheme.

2.3 Computation of Auxiliary Variable

To complete the definition of the method in one dimension, a procedure to compute the auxiliary variable values $q_{n,j}$ must be discussed. Since dependence on this variable exists only for the diffusive flux, the preceding sections provide a complete description of the DFR method for a pure advection problem.

To compute the auxiliary variable, a continuous solution function \tilde{u}_n^C is defined using Lagrange interpolating polynomials as

$$\tilde{u}_n^C = u_{n,0}^I \bar{\ell}_0 + \sum_{j=1}^{P+1} u_{n,j} \bar{\ell}_j + u_{n,P+2}^I \bar{\ell}_{P+2}, \quad (20)$$

where $u_{n,0}^I$ and $u_{n,P+2}^I$ are imposed common solution values at the left and right boundary flux points respectively. These common solution values are imposed at element boundaries to enforce desired continuity properties of \tilde{u}^C . The common solution values are computed as

$$u_{n,j}^I = U(u_L, u_R), \quad (21)$$

where $U(u_L, u_R)$ is a common solution function, typically associated with the chosen common viscous flux function F_{dif} . Differentiation of Eq. (20) yields

$$\frac{\partial \tilde{u}_n^C}{\partial r} = u_{n,L}^I \frac{d\bar{\ell}_0}{dr} + \sum_{j=1}^{P+1} u_{n,j} \frac{d\bar{\ell}_j}{dr} + u_{n,R}^I \frac{d\bar{\ell}_{P+2}}{dr} \quad (22)$$

which leads to the definition of the auxiliary variable values $q_{n,j}$ as

$$q_{n,j} = \frac{1}{J_n} \frac{\partial \tilde{u}_n^C}{\partial r} \Big|_{r=r_j} \quad (23)$$

Substitution of values from Eq. (23) into Eq. (14) define function \tilde{q}_n and completes the description of the DFR method in one dimension for advection–diffusion type problems.

2.4 Defining Characteristics of 1D DFR Scheme

The DFR scheme in one dimension has several defining characteristics which differentiate it from similar methods such as the standard FR scheme [16,34] or SD scheme [21,22]. First, unlike FR and SD, the DFR scheme uses a flux interpolant of degree $P+2$, leading to a flux derivative of degree $P+1$. This is in contrast to the other schemes which use flux interpolants

of degree $P+1$. The higher order flux interpolant enables the use of internal flux points that are coincident with the solution points, which differentiates the DFR scheme from the standard SD scheme. Compared to the FR scheme, the DFR scheme does not use correction functions to impose desired common solution and flux values on element boundaries. Instead, the DFR scheme imposes values at the element boundaries directly using an extended Lagrange interpolation procedure. These defining features will be used to guide the development of a new DFR scheme for triangles.

3 DFR in 2D on Triangular Elements

The following section develops the DFR scheme on triangles, which maintains many of the defining features of the one-dimensional formulation.

3.1 Preliminaries

Consider a 2D scalar conservation law

$$\frac{\partial u}{\partial t} + \nabla_{\mathbf{x}} \cdot \mathbf{f} = 0, \quad (24)$$

defined within a two-dimensional domain $\Omega \in \mathbb{R}^2$ where $\mathbf{x} = (x, y)$ is the spatial coordinate, t is time, $u = u(\mathbf{x}, t)$ is a scalar quantity and $\mathbf{f} = \mathbf{f}(u, \nabla_{\mathbf{x}} u) = (f_x, f_y)$ is a flux function which depends on the scalar and its gradient, where f_x and f_y refer to the components of the flux along in the x and y spatial dimensions respectively. For advection–diffusion, the flux can be split as $\mathbf{f} = \mathbf{f}_{adv} + \mathbf{f}_{dif}$, with $\mathbf{f}_{adv} = \mathbf{f}_{adv}(u)$ corresponding to the convective flux which depends only on the scalar u , and $\mathbf{f}_{dif} = \mathbf{f}_{dif}(u, \nabla_{\mathbf{x}} u)$ corresponding to the diffusive flux which depends on the scalar and its gradient. Next, Eq. (24) is split into a system of first-order equations as

$$\frac{\partial u}{\partial t} + \nabla_{\mathbf{x}} \cdot \mathbf{f}(u, \mathbf{q}) = 0, \quad (25)$$

$$\mathbf{q} - \nabla_{\mathbf{x}} u = 0, \quad (26)$$

with the introduction of a new variable, $\mathbf{q} = (q_x, q_y)$, which is referred to again as the auxiliary variable, where q_x and q_y refer to the components of \mathbf{q} along the x and y spatial dimensions respectively.

Next, consider partitioning the domain Ω into N non-overlapping triangular elements, such that $\Omega = \cup_{n=1}^N \Omega_n$ and define an approximate element local system

$$\frac{\partial u_n}{\partial t} + \nabla_{\mathbf{x}} \cdot \mathbf{f}_n = 0, \quad (27)$$

$$\mathbf{q}_n - \nabla_{\mathbf{x}} u_n = 0, \quad (28)$$

where $u_n = u_n(\mathbf{x}, t)$, $\mathbf{f}_n = \mathbf{f}_n(\mathbf{x}, t)$, and $\mathbf{q}_n = \mathbf{q}_n(\mathbf{x}, t)$ are piecewise polynomial functions within Ω_n , taking the value of zero elsewhere in the domain Ω . The global approximations to solution u and flux \mathbf{f} are defined as

$$u \approx \sum_{n=1}^N u_n, \quad \mathbf{f} \approx \sum_{n=1}^N \mathbf{f}_n. \quad (29)$$

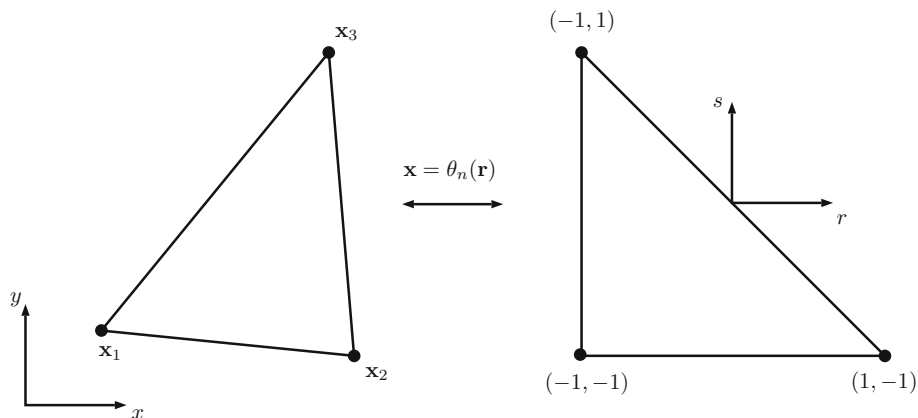


Fig. 1 Transformation to reference *right triangle*

As a requirement for conservation for two dimensions, the normal flux, $(\mathbf{f} \cdot \hat{\mathbf{n}})$, must be at least C^0 -continuous at element boundaries, where $\hat{\mathbf{n}}$ refers to the untransformed unit normal vector defined along the element boundaries.

To simplify the formulation, the elements Ω_n are each transformed to standard reference right triangular elements $\tilde{\Omega}_n$ via an isoparametric mapping function $\mathbf{x} = \theta_n(\mathbf{r})$ with associated geometric Jacobian matrix, \mathbf{J}_n , where $\mathbf{r} = (r, s)$ is the reference coordinate. A visual depiction of this mapping can be found in Fig. 1. Applying this mapping to Eqs. (27) and (28) yields a transformed system within each $\tilde{\Omega}_n$

$$\frac{\partial \tilde{u}_n}{\partial t} + \frac{1}{|\mathbf{J}_n|} \nabla_{\mathbf{r}} \cdot \tilde{\mathbf{f}}_n = 0, \quad (30)$$

$$\tilde{\mathbf{q}}_n - \nabla_{\mathbf{x}} u_n = 0, \quad (31)$$

where

$$\tilde{u}_n = \tilde{u}_n(\mathbf{r}, t) = u_n(\theta_n(\mathbf{r}), t), \quad (32)$$

$$\tilde{\mathbf{f}}_n = \tilde{\mathbf{f}}_n(\mathbf{r}, t) = |\mathbf{J}_n| \mathbf{J}_n^{-1} \mathbf{f}_n(\theta_n(\mathbf{r}), t) = (\tilde{f}_x, \tilde{f}_y), \quad (33)$$

$$\tilde{\mathbf{q}}_n = \tilde{\mathbf{q}}_n(\mathbf{r}, t) = \mathbf{q}_n(\theta_n(\mathbf{r}), t) = (\tilde{q}_x, \tilde{q}_y), \quad (34)$$

An important property of the transformation given by Eqs. (32)–(34) relating the untransformed divergence to the transformed divergence is

$$\nabla_{\mathbf{x}} \cdot \mathbf{f}_n = \frac{1}{|\mathbf{J}_n|} \nabla_{\mathbf{r}} \cdot \tilde{\mathbf{f}}_n. \quad (35)$$

Before continuing on to the development of the method, a key observation about the transformation of \mathbf{q}_n described by Eq. (34) should be made. In comparison to the transformation used for the standard FR formulation [36, 38], Eq. (34) is modified so that the components of $\tilde{\mathbf{q}}_n$, \tilde{q}_x and \tilde{q}_y , correspond to the untransformed gradient values via Eq. (31), instead of transformed gradient values. This modification is made to correspond to a new auxiliary variable computation formulated in the subsequent sections.

3.2 Procedure for First-Order Flux

We begin with the two-dimensional DFR procedure for a first-order flux on triangles, in the context of solving Eq. (30). Similar to what was done in the one-dimensional formulation, define a set of N_S solution points $\{\mathbf{r}_1, \mathbf{r}_2, \dots, \mathbf{r}_{N_S}\}$ in the interior of the standard triangular element where $N_S = \frac{1}{2}(P+1)(P+2)$ is the number of points required to interpolate a polynomial of degree P within the triangle. Next, define a set of N_F flux points $\{\mathbf{r}_1, \mathbf{r}_2, \dots, \mathbf{r}_{N_S}, \mathbf{r}_{N_S+1}, \dots, \mathbf{r}_{N_F}\}$ which includes the previously defined solution points and a number of additional points on the element boundaries. Note that again by definition, the flux points in the element interior and solution points are coincident. In a departure from the standard FR formulation on triangles [4, 37] and the SD–RT scheme [3, 23] which place $P+1$ points on each edge of the triangular element, consider placing $P+2$ points on each edge of the triangular element, which results in $N_F = N_S + N_{FB}$ where $N_{FB} = 3(P+2)$, the number of flux points on the element boundary. A depiction of the solution and flux point locations on the reference triangle can be found in Fig. 2.

The functions \tilde{u}_n and $\tilde{\mathbf{q}}_n$ are represented using scalar-valued interpolating polynomials as

$$\tilde{u}_n = \sum_{j=1}^{N_S} u_{n,j} \mathcal{L}_j, \quad (36)$$

$$\tilde{\mathbf{q}}_n = (\tilde{q}_{xn}, \tilde{q}_{yn}), \quad (37)$$

$$\tilde{q}_{xn} = \sum_{j=1}^{N_S} q_{xn,j} \mathcal{L}_j, \quad (38)$$

$$\tilde{q}_{yn} = \sum_{j=1}^{N_S} q_{yn,j} \mathcal{L}_j, \quad (39)$$

where $u_{n,j}$ are the solution value and $q_{xn,j}$ and $q_{yn,j}$ are the auxiliary variable values along each spatial dimension sampled at the solution point \mathbf{r}_j . \mathcal{L}_j are two-dimensional Lagrange polynomials defined using the solution points such that

$$\mathcal{L}_j(\mathbf{r}_i) = \delta_{i,j} \quad \text{for } i, j = 1, 2, \dots, N_S. \quad (40)$$

In particular, the \mathcal{L}_j are defined to form a basis in P_P , a two dimensional polynomial space of degree P . As done in the one-dimensional description, the procedure to compute the auxiliary variable values $q_{xn,j}$ and $q_{yn,j}$ will be discussed in the subsequent section.

In order to represent the flux function $\tilde{\mathbf{f}}_n$, a modified form of the flux interpolation method developed for the SD–RT scheme is used [3]. Unlike the method proposed in that work, this modified form enables the collocation of the solution point and internal flux point locations. As a preliminary step, define a two-dimensional Raviart–Thomas space [27] of degree P , denoted as RT_P as

$$RT_P = (P_P)^2 + \mathbf{r}P_P, \quad (41)$$

where $(P_P)^2$ denotes a two-dimensional vector space containing all vectors for which each component is a polynomial of at most degree P . The first key aspect of this space is that the dimension of RT_P is $(P+1)(P+3)$. The second key aspect of this space is the following property

$$\nabla \cdot \mathbf{v} \in P_P \quad \forall \mathbf{v} \in RT_P, \quad (42)$$

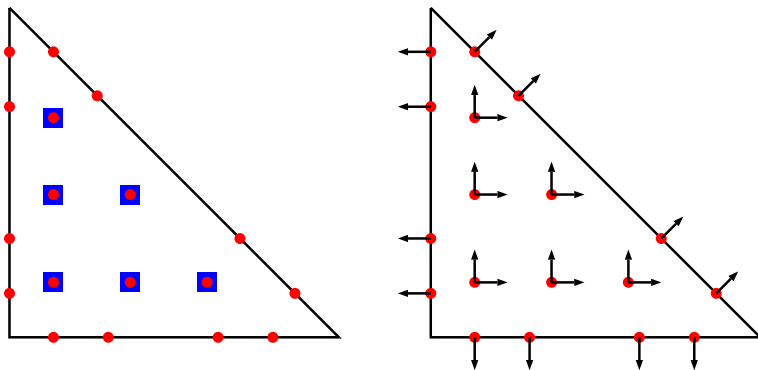


Fig. 2 Degrees of freedom on reference triangle for $P = 2$. The solution points are represented by *blue squares*, flux points are represented by *red circles*, and unit vectors for Raviart–Thomas flux interpolation are represented by *black arrows*

which states that the divergence of any vector field within the space RT_P is a polynomial of at most degree P . A characteristic of the DFR scheme in one dimension was the use of a flux interpolant of degree $P + 2$, with an associated derivative of degree $P + 1$. In an analogous fashion, consider representing the two-dimensional $\tilde{\mathbf{f}}$ using a basis spanning the space RT_{P+1} , which leads to an associated divergence of degree $P + 1$ via the property in Eq. (42).

First, define a set of vector-valued interpolation functions $\{\psi_1, \psi_2, \dots, \psi_{N_{RT}}\}$ which form a basis within RT_{P+1} , where $N_{RT} = (P + 2)(P + 4)$, the number of degrees of freedom required to form a basis of this degree. Each degree of freedom is comprised of a coordinate location s_j and a unit vector \mathbf{w}_j . The interpolation functions ψ_j are defined such that

$$\psi_j(s_i) \cdot \mathbf{w}_i = \delta_{i,j}. \quad (43)$$

To generate the N_{RT} required degrees of freedom, associate two unit vectors \mathbf{e}_r and \mathbf{e}_s with each internal flux point, and a single unit vector oriented in the outward transformed normal direction on the reference triangle, $\hat{\mathbf{n}}_j$, with each boundary flux point. The vectors \mathbf{e}_r and \mathbf{e}_s refer to unit vectors oriented in the r and s transformed spatial directions respectively. A visual depiction of the degrees of freedom used on the reference triangle can be found Fig. 2. Thus, each internal flux point generates two degrees of freedom while each boundary flux point generates one degree of freedom, for a total of $2N_s + N_{FB} = (P + 2)(P + 4)$ degrees of freedom. An important point to note is that the increased number of flux points on the element boundaries provides a means to meet the degree of freedom requirements for RT_{P+1} without modifying the number of internal flux points. This is in contrast to the SD–RT scheme, where a number of non-collocated flux points are defined within the element in order to meet the reduced degree of freedom requirements of a Raviart–Thomas space of one degree lower, RT_P .

Now, the function $\tilde{\mathbf{f}}_n$ can be represented as

$$\tilde{\mathbf{f}}_n = \sum_{j=1}^{N_{RT}} f_j \psi_j, \quad (44)$$

with

$$f_j = \begin{cases} |\mathbf{J}_{n,j}| \mathbf{J}_{n,j}^{-1} \mathbf{f}_{n,j} \cdot \mathbf{e}_r & \text{if } j \leq N_s \\ |\mathbf{J}_{n,j}| \mathbf{J}_{n,j}^{-1} \mathbf{f}_{n,j-N_s} \cdot \mathbf{e}_s & \text{if } N_s < j \leq 2N_s \\ \|\mathbf{n}_j\| f_{n,j}^I & \text{if } j > 2N_s \end{cases} \quad (45)$$

where $f_{n,j}^I$ is the imposed common normal flux and \mathbf{n}_j is the untransformed normal at boundary flux point \mathbf{r}_j . In Eq. (45), the first two cases correspond to the degrees of freedom located at the solution points, while the last case pertains to the degrees of freedom located at the boundary flux points. The relationship between the transformed and untransformed normals is given by

$$\mathbf{n}_j = \|\mathbf{n}_j\| \hat{\mathbf{n}}_j = |\mathbf{J}_{n,j}| \mathbf{J}_{n,j}^{-T} \hat{\mathbf{n}}_j. \quad (46)$$

As before, the common interface flux values $f_{n,j}^I$ can be split into two components

$$f_{n,j}^I = F_{adv}(u_-, u_+) + F_{dif}(u_-, u_+, q_-, q_+), \quad (47)$$

where the subscript \square_- refers to values at the flux point computed using information local to element n , the subscript \square_+ refers to values computed at the same shared flux point computed using information from the adjoining element, and F_{adv} and F_{dif} are multi-dimensional analogs of the common flux functions listed in the previous section. Applying the Rusanov flux function, F_{adv} takes the form

$$F_{adv}(u_-, u_+) = \frac{1}{2} [f_{adv}(u_-) + f_{adv}(u_+)] \cdot \hat{\mathbf{n}}_- + \frac{c}{2} [u_- - u_+], \quad (48)$$

where c is an approximation of the wavespeed and $\hat{\mathbf{n}}_-$ is the outward unit normal, relative to element n , at the flux point. Applying the LDG flux function, F_{dif} takes the form

$$\begin{aligned} F_{dif}(u_-, u_+, q_-, q_+) = \hat{\mathbf{n}}_- \cdot \left\{ \frac{1}{2} [f_{dif}(u_-, q_-) + f_{dif}(u_+, q_+)] \right. \\ \left. + \beta [f_{dif}(u_-, q_-) \cdot \hat{\mathbf{n}}_- + f_{dif}(u_+, q_+) \cdot \hat{\mathbf{n}}_+] \right. \\ \left. + \tau [u_- \hat{\mathbf{n}}_- - u_+ \hat{\mathbf{n}}_+] \right\}, \end{aligned} \quad (49)$$

where $\hat{\mathbf{n}}_+$ is the inward unit normal at the flux point, relative to element n , β is a switch parameter controlling upwinding, and τ is a penalty parameter.

Substitution of Eq. (44) into Eq. (30) yields the following semi-discrete equation for the DFR scheme on triangles

$$\frac{d\tilde{u}_n}{dt} + \frac{1}{|\mathbf{J}_n|} \sum_{j=1}^{N_{RT}} f_j (\nabla_{\mathbf{r}} \cdot \boldsymbol{\psi}_j) = 0. \quad (50)$$

Equation (50) describes a system of ordinary differential equations in t which can be marched forward in time using a number of time integration schemes.

3.3 Computation of Auxiliary Variable

To complete the definition of the method on triangles, a procedure to compute the auxiliary variable values $\tilde{q}_{n,j}$ must be discussed. For a pure advection problem, no dependence on the auxiliary variable exists and the previous section provides a complete description of the DFR method on triangles in this case.

For the one-dimensional DFR scheme, the procedure to compute the auxiliary variable is to form a continuous solution function with imposed common solution values on the boundaries and compute the gradient directly using Lagrange interpolation functions. On triangles however, a suitable representation for the continuous solution has not been defined. The scalar field representation using the two-dimensional Lagrange polynomials, \mathcal{L}_j , used in Eq. (36) does not include element boundary data and cannot be used to impose desired common solution values on the resulting interpolant. To address this, one might consider forming a larger Lagrange interpolation basis using all the flux points including those on the boundary; however, the number of degrees of freedom, N_F , generated in this case does not, in general, equal the number of degrees of freedom required to represent a polynomial over the triangle of any specific degree. For these reasons, a new procedure to compute the auxiliary variable is developed.

In the previous section, a procedure to compute the divergence of a continuous flux field was defined. Comparing Eqs. (30) and (50) gives the relation

$$\frac{1}{|\mathbf{J}_n|} \nabla_{\mathbf{r}} \cdot \tilde{\mathbf{f}}_n = \frac{1}{|\mathbf{J}_n|} \sum_{j=1}^{N_{RT}} f_j (\nabla_{\mathbf{r}} \cdot \boldsymbol{\psi}_j), \quad (51)$$

with the f_j defined in Eq. (45). Application of the property given in Eq. (35) results in

$$\nabla_{\mathbf{x}} \cdot \mathbf{f}_n = \frac{1}{|\mathbf{J}_n|} \sum_{j=1}^{N_{RT}} f_j (\nabla_{\mathbf{r}} \cdot \boldsymbol{\psi}_j). \quad (52)$$

Let $\tilde{\mathbf{f}}_n$ be a linear advective flux, $\tilde{\mathbf{f}}_n = \mathbf{a} u_n$, where \mathbf{a} is a vector wavespeed and u_n is the scalar valued solution. Substitution of this flux function into Eq. (51) and applying the product rule to the left hand side yields

$$u_n (\nabla_{\mathbf{x}} \cdot \mathbf{a}) + \nabla_{\mathbf{x}} u_n \cdot \mathbf{a} = \frac{1}{|\mathbf{J}_n|} \sum_{j=1}^{N_{RT}} f_j (\nabla_{\mathbf{r}} \cdot \boldsymbol{\psi}_j). \quad (53)$$

If the wavespeed is set as $\mathbf{a} = \mathbf{e}_x$, where \mathbf{e}_x refers to a unit vector oriented in the x spatial dimension, then Eq. (53) becomes

$$\frac{\partial u_n}{\partial x} = \frac{1}{|\mathbf{J}_n|} \sum_{j=1}^{N_{RT}} f_j (\nabla_{\mathbf{r}} \cdot \boldsymbol{\psi}_j), \quad (54)$$

where f_j is now defined as

$$f_j = \begin{cases} |\mathbf{J}_{n,j}| \mathbf{J}_{n,j}^{-1} \mathbf{e}_x u_{n,j} \cdot \mathbf{e}_r & \text{if } j \leq N_s \\ |\mathbf{J}_{n,j}| \mathbf{J}_{n,j}^{-1} \mathbf{e}_x u_{n,j-N_s} \cdot \mathbf{e}_s & \text{if } N_s < j \leq 2N_s \\ ||\mathbf{n}_j|| f_{n,j}^I & \text{if } j > 2N_s \end{cases} \quad (55)$$

For this computation, the imposed common interface flux values f_j^I are defined as

$$f_{n,j}^I = \mathbf{e}_x u_{n,j}^I \cdot \hat{\mathbf{n}}_j, \quad (56)$$

where $u_{n,j}^I$ corresponds to the desired common solution value. The common solution values $u_{n,j}^I$ are set via a common solution function $U(u_-, u_+)$. For the LDG approach, this function is defined as

$$U(u_-, u_+) = \frac{1}{2} [u_- + u_+] - \boldsymbol{\beta} \cdot [u_- \hat{\mathbf{n}}_- + u_+ \hat{\mathbf{n}}_+]. \quad (57)$$

Equation (56) describes an outward normal flux computed using the imposed common solution value at the given flux point and the prescribed wavespeed, e_x . Imposing this common interface flux serves as a mechanism to indirectly enforce a common solution value at the boundary flux points. Eqs. (45), (54) and (56) provide a complete definition of one component of the solution gradient $\frac{\partial u_n}{\partial x}$, computed using the flux divergence operation developed in the previous section. This component corresponds exactly with the first component, q_{x_n} , of the auxiliary variable $\tilde{q}_{n,j}$ via Eq. (31). To compute the remaining component, q_{y_n} , the same procedure is carried out, with $\mathbf{a} = \mathbf{e}_y$, where \mathbf{e}_y refers to a unit vector oriented in the y spatial dimension. These values are substituted into Eq. (37) to Eq. (39) to complete the description of the DFR on triangles for advection–diffusion problems.

4 Von Neumann Analysis

To better understand the linear stability properties of the DFR scheme on triangles, a von Neumann stability analysis of the scheme applied to a linear advection problem is performed. The analysis here follows similar methods used to analyze linear stability properties of the SD scheme by Van den Abeele [1], the ESFR scheme on triangles by Castonguay et al. [4], and the SD–RT scheme by Balan et al. [3].

4.1 Semi-Discrete System

Consider the 2D linear advection equation

$$\frac{\partial u}{\partial t} + \nabla_x \cdot (\mathbf{a}u) = 0, \quad (58)$$

where $\mathbf{a} = \|\mathbf{a}\|(\cos \psi, \sin \psi)$ and $u(\mathbf{x}, t)$ is a scalar quantity. This equation is discretized on a uniform skewed mesh, as depicted in Fig. 3, with skew angle ϕ . Each grid element, indexed by (i, j) in the associated figure, is comprised of two triangular elements. The grid pattern can be described by two vectors, $\mathbf{H}_1 = (H_{1x}, H_{1y}) = (h, 0)$, and $\mathbf{H}_2 = (H_{2x}, H_{2y}) = (h \cos \phi, h \sin \phi)$, where h denotes the horizontal element edge length.

Application of the DFR scheme on triangles to Eq. (58) using the Rusanov interface flux function yields the following semi-discrete equation

$$\frac{d}{dt} \mathbf{U}_{i,j} = \frac{\|\mathbf{a}\|}{h} \left[\mathbf{C}^{(0,0)} \mathbf{U}_{i,j} + \mathbf{C}^{(-,0)} \mathbf{U}_{i-1,j} + \mathbf{C}^{(0,-)} \mathbf{U}_{i,j-1} + \mathbf{C}^{(+,0)} \mathbf{U}_{i+1,j} + \mathbf{C}^{(0,+)} \mathbf{U}_{i,j+1} \right], \quad (59)$$

where the $\mathbf{U}_{i,j}$ are vectors of dimension $2N_s$ containing the combined scalar solution values for the two triangular elements comprising each mesh element (i, j) . The matrices $\mathbf{C}^{(\cdot,\cdot)}$ are each of dimension $2N_s \times 2N_s$ and are a function of the advection angle ψ , the skew angle ϕ , and the location of the solution and flux points used in the DFR discretization.

Next, assume the solution $\mathbf{U}_{i,j}$ takes the form of a 2D plane wave

$$\mathbf{U}_{i,j} = \tilde{\mathbf{U}} \exp(\mathcal{I}k[(iH_{1x} + jH_{2x}) \cos \theta + (iH_{1y} + jH_{2y}) \sin \theta]), \quad (60)$$

where $\mathcal{I} = \sqrt{-1}$, k is the wave number, θ is the wave orientation angle, and $\tilde{\mathbf{U}}$ is a complex vector of dimension $2N_s$. Substitution of Eq. (60) into Eq. (59) with periodic boundaries yields a semi-discrete equation for $\tilde{\mathbf{U}}$

$$\frac{d}{dt} \tilde{\mathbf{U}} = \mathbf{Q} \tilde{\mathbf{U}} \quad (61)$$

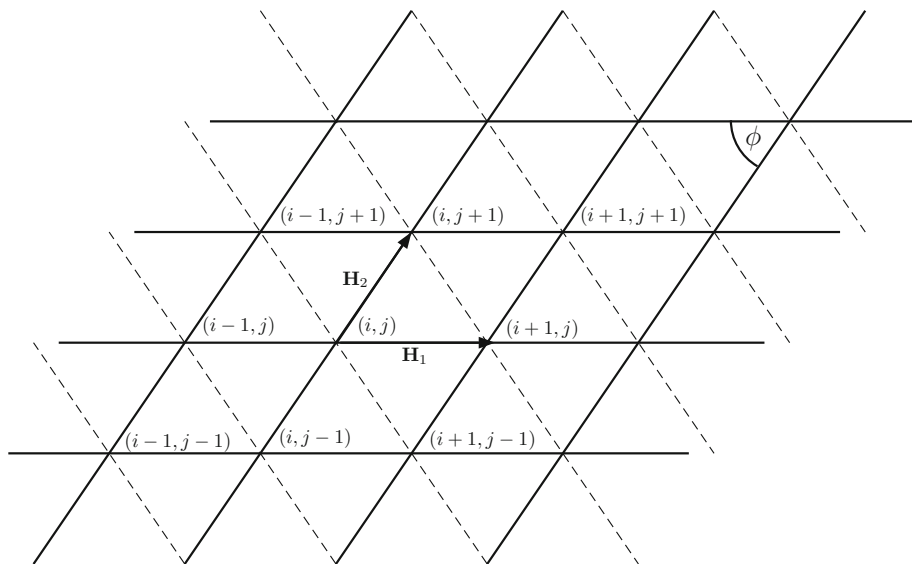


Fig. 3 Grid setup for von Neumann analysis

where

$$\begin{aligned}
 \mathbf{Q} = & \frac{\|\mathbf{a}\|}{h} [\mathbf{C}^{(0,0)} \\
 & + \mathbf{C}^{(-,0)} \exp(-\mathcal{I}k[H_{1x} \cos \theta + H_{1y} \sin \theta]) \\
 & + \mathbf{C}^{(0,-)} \exp(-\mathcal{I}k[H_{2x} \cos \theta + H_{2y} \sin \theta]) \\
 & + \mathbf{C}^{(+,0)} \exp(\mathcal{I}k[H_{1x} \cos \theta + H_{1y} \sin \theta]) \\
 & + \mathbf{C}^{(0,+)} \exp(\mathcal{I}k[H_{2x} \cos \theta + H_{2y} \sin \theta])]
 \end{aligned} \quad (62)$$

For this analysis, we consider the case with unit wavespeed, $\|\mathbf{a}\| = 1$ and unit edge length, $h = 1$. Within this context, a DFR scheme is considered linearly stable if the real component of the eigenvalues, λ , of the matrix \mathbf{Q} are non-positive over all wavenumbers $k \in [0, 2\pi]$, skew angles $\phi \in (0, \pi)$, advection angles $\psi \in [0, \pi]$ and wave orientation angles $\theta \in [0, \pi]$.

4.2 Results and Analysis

The maximum real component of the eigenvalues over discretized ranges of k , ϕ , ψ , and θ were computed numerically for various \mathbf{Q} matrices, associated with several variations of the DFR scheme on triangles for the advection equation. These variations are identified by the location of the collocated internal solution and flux points as well as the degree of polynomial interpolant, P , used to represent the solution. For all variations, the boundary flux points are fixed to the Gauss-Legendre points along each element edge.

As a baseline, the internal collocation points were set as the quadrature points on triangles reported by Williams and Shunn [36]. For convenience, these points will be referred to as the WS points for the remainder of the paper. This choice is informed by previous results for the SD-RT scheme where linear stability was achieved via collocation of the internal flux points with optimal quadrature points [3], up to their scheme utilizing a polynomial solution

representation of $P = 3$. In fact, the WS points up to $P = 2$ correspond exactly to the optimal quadrature points used in that study which resulted in linearly stable schemes. Using the WS points, the von Neumann analysis reveals that the DFR scheme is linearly stable over the range of parameters tested for the scheme using $P = 1$ and $P = 2$ solution interpolants but is weakly unstable for the scheme using $P = 3$ and $P = 4$ solution interpolants. Due to the increased order of the flux interpolant used in the DFR scheme, the flux interpolants for the DFR scheme using $P = 1$ and $P = 2$ correspond to the interpolants used for the SD–RT scheme using $P = 2$ and $P = 3$. Considering this, the linear stability results at $P = 1$ and $P = 2$ are consistent with the results reported for the SD–RT scheme. Stability results for the SD–RT scheme were not reported beyond the scheme using $P = 3$.

Further investigation into the weak instabilities discovered for $P = 3$ and $P = 4$ was carried out. To simplify the analysis, the parameters ranges were reduced to four skew angles, $\phi = 30^\circ, 60^\circ, 90^\circ, 120^\circ$, and the wave orientation angle was set equal to the advection angle, $\theta = \psi$. The results of this analysis for $P = 3$ and $P = 4$ can be seen in Figs. 4 and 5 respectively. Each figure shows the maximum real component of the eigenvalues over all tested wavenumbers as a function of the advection angle, with separate plots for each skew angle. When using the WS points for both polynomial orders, the maximum real eigenvalue component has small positive peaks at grid-aligned advection angles, with reduced but still positive values at all other angles. The positive values indicate linear instability; however, the small magnitudes suggest that the instability is weak.

The instabilities observed using WS points motivated a search for alternative internal point locations for which these instabilities are reduced or eliminated. For the number of internal points corresponding to the $P = 3$ and $P = 4$ DFR schemes, 10 points and 15 points respectively, Witherden et al. [39] reported several alternative quadrature point locations which maintain the same optimal integration order as those reported by Williams and Shunn. These alternative point locations were generally found to result in schemes which were highly unstable for the tested polynomial orders with a few exceptions; one set of points for $P = 3$, the “truncation error optimal” points as defined by Witherden et al., resulted in a scheme with reduced peak maximum real eigenvalue components at grid-aligned advection angles relative to the WS point results and numerically zero maximum real eigenvalue components at other angles. This result can be observed along with the WS point results in Fig. 4. These points will be referred to as WV points for the remainder of the paper.

In order to find internal point locations which further reduce the maximum real eigenvalue components at all advection angles, a feasibility optimization problem was formulated and solved numerically. Before stating the optimization problem, a parameterization of the internal solution point locations must be defined. For this optimization, the parameterization using symmetry orbits described by Witherden et al. [39] was utilized. In brief, this parameterization defines the location of rotationally-symmetric internal point locations on a triangle using a reduced number of scalar coefficients which are expanded to obtain all point locations. The full description of this parameterization procedure is left to the cited reference.

For a set skew angle $\phi = 90^\circ$, the feasibility problem solved is

$$\begin{aligned} & \underset{\alpha}{\text{minimize}} && 0 \\ & \text{subject to} && \max_{k, \psi}(\lambda_r) \leq \epsilon. \end{aligned}$$

where α are the parameters defining the internal point locations, λ_r are the real components of the eigenvalues of the matrices \mathcal{Q} , and ϵ is a target maximum threshold for the maximum real component of the eigenvalues. For this study, ϵ was set to a threshold value of 10^{-10} . This feasibility problem was solved numerically for $P = 3$ and $P = 4$ using the WS points

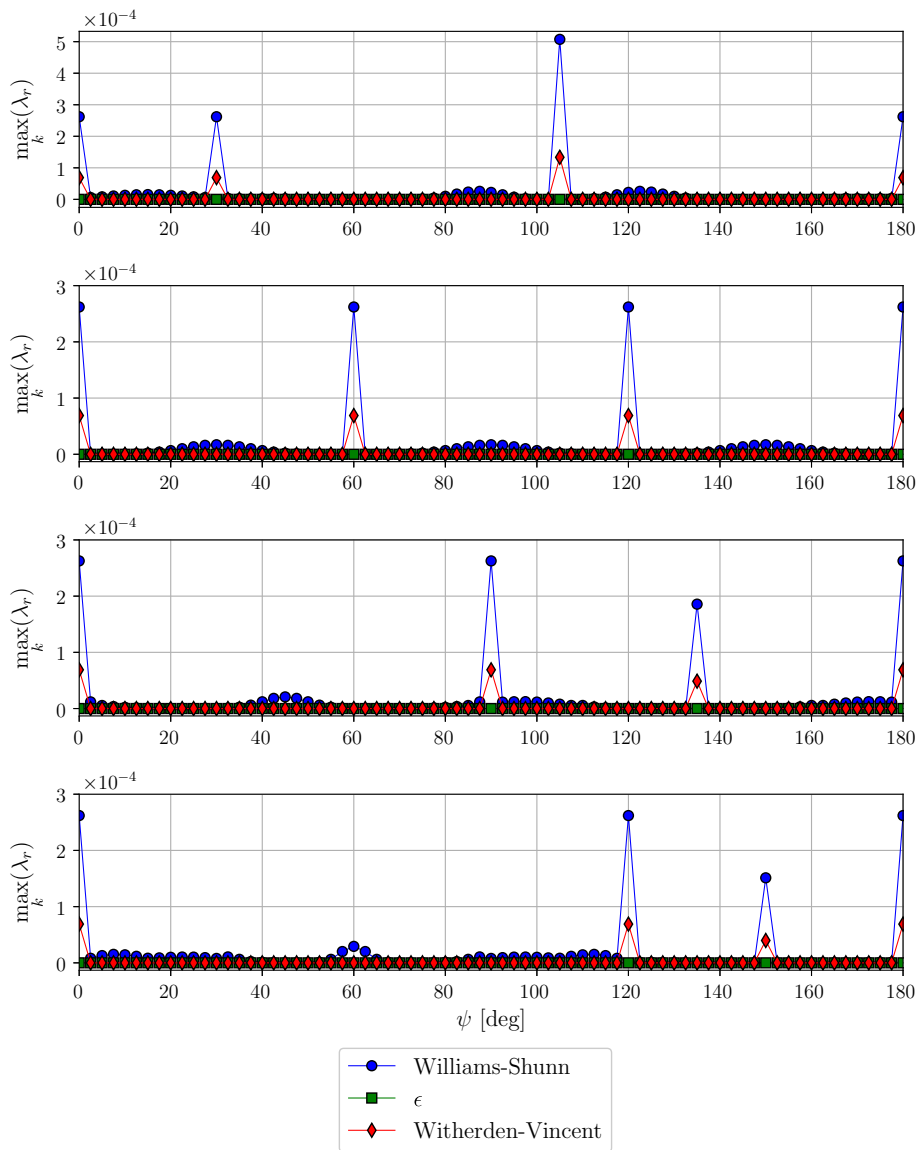


Fig. 4 Von Neumann results for $P = 3$, $\phi = 30^\circ, 60^\circ, 90^\circ, 120^\circ$ (top to bottom)

for initialization and resulted in an additional set of internal points for $P = 3$ and $P = 4$. These point locations will be referred to as ϵ points for the remainder of the paper. These point locations are listed in Table 17 in barycentric coordinates. Barycentric coordinates are related to coordinate locations on the reference right triangle via the formula

$$\mathbf{r} = \begin{bmatrix} -1 & 1 & -1 \\ -1 & -1 & 1 \end{bmatrix} \boldsymbol{\xi}. \quad (63)$$

The results for these points can be observed in Figs. 4 and 5 at the specified configurations. These plots show that the ϵ points significantly reduce the maximum real eigenvalue

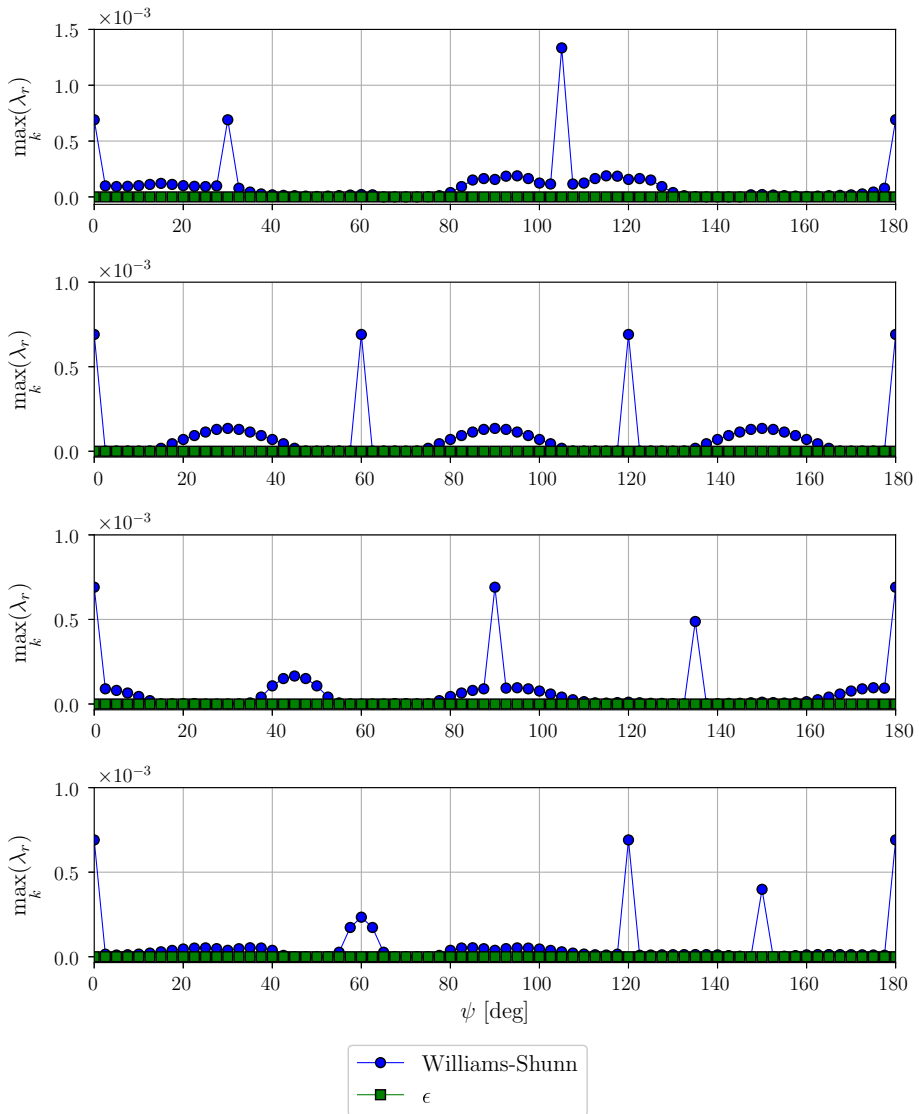


Fig. 5 Von Neumann results for $P = 4$, $\phi = 30^\circ, 60^\circ, 90^\circ, 120^\circ$ (top to bottom)

component across all advection angles for $P = 3$ and $P = 4$. We do note that the optimization problem was limited to a single skew angle and for plane wave angles set equal to the advection angle. The figures indicate that, for several additional skew angles, the reduction of the maximum real eigenvalue component holds.

5 Numerical Experiments

This section contains the results of several linear and nonlinear test cases discretized using the newly developed DFR scheme on triangles. The common interface flux and solution

computations are carried out using the Rusanov flux function, as described by Eq. (48), and the LDG solution and flux functions, described by Eqs. (49) and (57). Additionally, the parameters for the LDG flux are set as $\beta = \frac{1}{2}\hat{n}_-$ and $\tau = 0.1$. These values were set to be consistent with similar studies carried out for the standard FR scheme [35, 38].

5.1 Linear Advection–Diffusion

In this section, we apply the DFR formulation on triangles to a 2D linear advection–diffusion problem

$$\frac{\partial u}{\partial t} + \nabla_{\mathbf{x}} \cdot (\mathbf{a}u - b\nabla_{\mathbf{x}}u) = 0, \quad (64)$$

defined in a square domain $\Omega \in [-1, 1] \times [-1, 1]$ with periodic boundary conditions, where $\mathbf{a} = (a_x, a_y) = ||\mathbf{a}||(\cos \psi, \sin \psi)$ is the advection velocity vector, b is the scalar diffusion coefficient and $u(\mathbf{x}, t)$ is a conserved scalar quantity. Application of the following initial condition

$$u(\mathbf{x}, 0) = \sin(\pi x) \sin(\pi y), \quad (65)$$

results in an analytic solution given by

$$u_e(\mathbf{x}, t) = e^{-2b\pi^2 t} \sin(\pi[x - a_x t]) \sin(\pi[y - a_y t]). \quad (66)$$

This definition enables the computation of the L2 error defined as

$$E_{L2}(t) = \sqrt{\int_{\Omega} (u(\mathbf{x}, t) - u_e(\mathbf{x}, t))^2 d\mathbf{x}}, \quad (67)$$

which is computed numerically using high strength element-wise quadrature. In all cases in this section, time is discretized using a standard RK4 scheme and the reported error is computed at $t = 1$. For each case, the timestep size is chosen to be sufficiently small so that spatial orders are dominant.

This test case is carried out across several configurations of polynomial order, P , advection angle, ψ , and on regular and irregular grids. Examples of the regular and irregular grids used can be seen in Fig. 6. For each configuration of the problem, the order of accuracy is computed using a reference grid length of $h = 2/N$ for the regular grids, and $h = 1/\sqrt{N_{\text{eles}}}$ for the irregular grids. The reported order is the result of a least-squares linear fit through the error results obtained at each grid resolution. For all orders, results using WS internal point locations are reported. For $P = 3$ and $P = 4$, results for the WV and ϵ points discussed in the previous section are also reported.

The order of accuracy results from the test case in a pure advection configuration ($||\mathbf{a}|| = 1$, $b = 0$) can be found in Tables 1, 2, 3 and 4. A few interesting observations can be made for this case. On regular grids at a grid-aligned advection angle $\psi = 0^\circ$, the order of accuracy exhibited by the scheme is suboptimal, achieving only an order of P . However, the order of accuracy increases to the expected order of $P + 1$ across most other cases, exhibiting little to no reduction in order at $\psi = 0^\circ$ when using irregular grids.

An exception to these findings are the results using the ϵ points for $P = 3$ which exhibit a suboptimal order of accuracy for all configurations. Previous results reported in literature for FR schemes have shown that the choice of correction function can result in schemes exhibiting reduced order of accuracy [5, 33]. In the current context, setting the location of the internal points can be considered an analogous mechanism in controlling the numerical

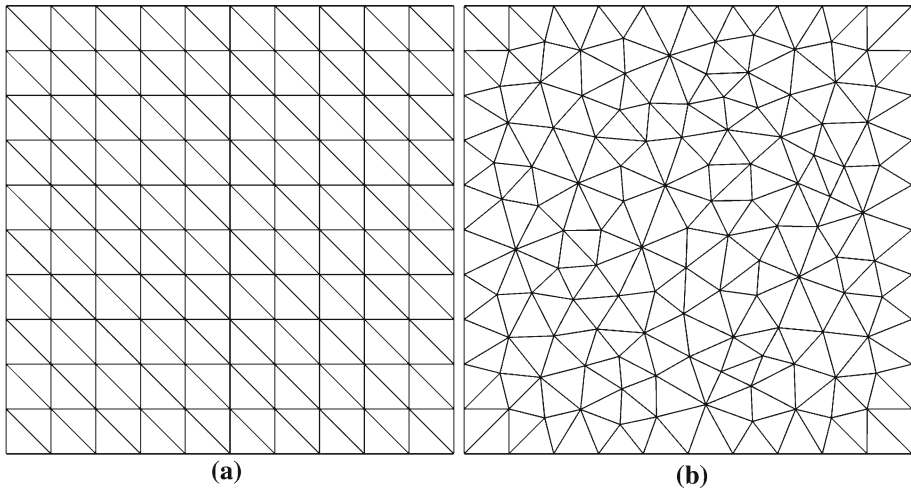


Fig. 6 Examples of meshes used for linear advection–diffusion test cases. **a** Regular Grid, $N = 10$. **b** Irregular Grid, $N_{\text{les}} = 252$

Table 1 Linear advection results on regular grids using Williams-Shunn points

N	$P = 1$	$P = 2$	$P = 3$	$P = 4$
$\psi = 0^\circ$				
10	6.401×10^{-2}	1.315×10^{-2}	1.813×10^{-3}	1.698×10^{-4}
20	2.730×10^{-2}	3.351×10^{-3}	2.345×10^{-4}	1.101×10^{-5}
30	1.762×10^{-2}	1.502×10^{-3}	7.024×10^{-5}	2.198×10^{-6}
40	1.308×10^{-2}	8.489×10^{-4}	2.979×10^{-5}	6.992×10^{-7}
Order	1.149 ± 0.033	1.977 ± 0.002	2.963 ± 0.005	3.961 ± 0.006
$\psi = 30^\circ$				
10	5.221×10^{-2}	3.657×10^{-3}	2.961×10^{-4}	1.960×10^{-5}
20	1.183×10^{-2}	4.459×10^{-4}	1.733×10^{-5}	5.837×10^{-7}
30	5.084×10^{-3}	1.316×10^{-4}	3.512×10^{-6}	8.039×10^{-8}
40	2.820×10^{-3}	5.547×10^{-5}	1.104×10^{-6}	1.836×10^{-8}
Order	2.107 ± 0.015	3.022 ± 0.006	4.031 ± 0.024	5.019 ± 0.026

properties of the resulting scheme. With this in mind, this particular result is not entirely unexpected.

The order of accuracy results from the test case in a pure diffusion configuration ($\|a\| = 0$, $b = 0.1$) can be found in Tables 5, 6, 7 and 8. For this case, using WS points results in the expected $P + 1$ order of accuracy across all tested P on regular and irregular grids. The same result is obtained for $P = 3$ using WV points. The results for $P = 4$ using the ϵ points shows a slight reduction in order on the regular grids but recovers the optimal order of $P + 1$ on the irregular grids. For $P = 3$ using the ϵ points, a significant degradation in order of accuracy, as low as $P - 1$, occurs. This gives further indication that the scheme resulting from these points suffers from poor numerical performance.

Table 2 Linear advection results on regular grids using Witherden-Vincent and ϵ points

N	$P = 3$ (WV)	$P = 3$ (ϵ)	$P = 4$ (ϵ)
$\psi = 0^\circ$			
10	1.877×10^{-3}	1.835×10^{-3}	1.730×10^{-4}
20	2.428×10^{-4}	2.372×10^{-4}	1.121×10^{-5}
30	7.270×10^{-5}	7.100×10^{-5}	2.238×10^{-6}
40	3.083×10^{-5}	3.011×10^{-5}	7.118×10^{-7}
Order	2.963 ± 0.005	2.964 ± 0.005	3.962 ± 0.006
$\psi = 30^\circ$			
10	3.003×10^{-4}	3.479×10^{-4}	1.993×10^{-5}
20	1.753×10^{-5}	2.895×10^{-5}	5.999×10^{-7}
30	3.537×10^{-6}	7.731×10^{-6}	8.261×10^{-8}
40	1.115×10^{-6}	3.112×10^{-6}	1.911×10^{-8}
Order	4.035 ± 0.024	3.410 ± 0.072	5.004 ± 0.023

Table 3 Linear advection results on irregular grids using Williams-Shunn points

N_{eles}	$P = 1$	$P = 2$	$P = 3$	$P = 4$
$\psi = 0^\circ$				
68	1.313×10^{-1}	1.720×10^{-2}	2.865×10^{-3}	2.815×10^{-4}
252	3.504×10^{-2}	2.765×10^{-3}	3.496×10^{-4}	1.341×10^{-5}
1042	8.211×10^{-3}	3.241×10^{-4}	1.936×10^{-5}	3.897×10^{-7}
2352	3.930×10^{-3}	9.073×10^{-5}	4.574×10^{-6}	4.549×10^{-8}
Order	1.992 ± 0.028	2.962 ± 0.049	3.687 ± 0.126	4.924 ± 0.086
$\psi = 30^\circ$				
68	1.202×10^{-1}	1.757×10^{-2}	2.149×10^{-3}	2.695×10^{-4}
252	3.303×10^{-2}	2.555×10^{-3}	1.634×10^{-4}	1.061×10^{-5}
1042	7.860×10^{-3}	3.274×10^{-4}	1.135×10^{-5}	3.153×10^{-7}
2352	3.540×10^{-3}	9.529×10^{-5}	2.115×10^{-6}	3.896×10^{-8}
Order	1.994 ± 0.008	2.937 ± 0.015	3.885 ± 0.040	4.982 ± 0.026

The order of accuracy results from the test case in an advection–diffusion configuration ($\|a\| = 1$, $b = 0.1$) can be found in Tables 9, 10, 11 and 12. The advection–diffusion results follow a similar trend to the results on a pure diffusion problem, including the slight order reduction in the case of $P = 4$ and significant reduction for $P = 3$ when using the ϵ points. However, unlike in the case of pure advection, the order of accuracy is observed to be insensitive to the advection angle.

5.2 Navier–Stokes

To assess the performance of the DFR formulation on triangles for nonlinear fluxes, the numerical scheme is applied to the compressible Navier–Stokes (NS) equations for two test problems: 2D Couette flow and viscous flow over a 2D cylinder.

Table 4 Linear advection results on irregular grids using Witherden-Vincent and ϵ points

N_{eles}	$P = 3$ (WV)	$P = 3$ (ϵ)	$P = 4$ (ϵ)
$\psi = 0^\circ$			
68	2.945×10^{-3}	2.935×10^{-3}	2.886×10^{-4}
252	3.615×10^{-4}	3.587×10^{-4}	1.374×10^{-5}
1042	2.014×10^{-5}	2.134×10^{-5}	3.937×10^{-7}
2352	4.760×10^{-6}	5.298×10^{-6}	4.715×10^{-8}
Order	3.680 ± 0.127	3.616 ± 0.111	4.923 ± 0.081
$\psi = 30^\circ$			
68	2.200×10^{-3}	2.237×10^{-3}	2.714×10^{-4}
252	1.676×10^{-4}	1.840×10^{-4}	1.076×10^{-5}
1042	1.166×10^{-5}	1.519×10^{-5}	3.163×10^{-7}
2352	2.182×10^{-6}	3.625×10^{-6}	3.926×10^{-8}
Order	3.881 ± 0.040	3.617 ± 0.052	4.984 ± 0.025

Table 5 Linear diffusion results on regular grids using Williams-Shunn points

N	$P = 1$	$P = 2$	$P = 3$	$P = 4$
10	1.045×10^{-2}	4.822×10^{-4}	2.882×10^{-5}	1.698×10^{-6}
20	2.639×10^{-3}	5.521×10^{-5}	1.801×10^{-6}	5.363×10^{-8}
30	1.171×10^{-3}	1.601×10^{-5}	3.557×10^{-7}	7.077×10^{-9}
40	6.573×10^{-4}	6.703×10^{-6}	1.126×10^{-7}	1.681×10^{-9}
Order	1.995 ± 0.004	3.086 ± 0.017	4.000 ± 0.000	4.990 ± 0.002

Table 6 Linear diffusion results on regular grids using Witherden-Vincent and ϵ points

N	$P = 3$ (WV)	$P = 3$ (ϵ)	$P = 4$ (ϵ)
10	3.090×10^{-5}	1.420×10^{-4}	1.798×10^{-6}
20	1.910×10^{-6}	3.520×10^{-5}	6.434×10^{-8}
30	3.766×10^{-7}	1.566×10^{-5}	9.975×10^{-9}
40	1.191×10^{-7}	8.812×10^{-6}	2.794×10^{-9}
Order	4.010 ± 0.002	2.005 ± 0.003	4.676 ± 0.057

Table 7 Linear diffusion results on irregular grids using Williams-Shunn points

N_{eles}	$P = 1$	$P = 2$	$P = 3$	$P = 4$
68	1.965×10^{-2}	1.986×10^{-3}	2.312×10^{-4}	1.980×10^{-5}
252	5.532×10^{-3}	2.625×10^{-4}	1.558×10^{-5}	6.705×10^{-7}
1042	1.460×10^{-3}	3.333×10^{-5}	8.635×10^{-7}	2.240×10^{-8}
2352	6.710×10^{-4}	9.440×10^{-6}	1.709×10^{-7}	2.679×10^{-9}
Order	1.903 ± 0.008	3.004 ± 0.027	4.073 ± 0.018	4.996 ± 0.058

Table 8 Linear diffusion results on irregular grids using Witherden-Vincent and ϵ points

N	$P = 3$ (WV)	$P = 3$ (ϵ)	$P = 4$ (ϵ)
68	2.377×10^{-4}	3.021×10^{-4}	2.003×10^{-5}
252	1.601×10^{-5}	5.362×10^{-5}	7.013×10^{-7}
1042	8.853×10^{-7}	1.291×10^{-5}	2.669×10^{-8}
2352	1.751×10^{-7}	5.668×10^{-6}	3.459×10^{-9}
Order	4.075 ± 0.018	2.223 ± 0.109	4.854 ± 0.074

Table 9 Linear advection-diffusion results on regular grids using Williams-Shunn points

N	$P = 1$	$P = 2$	$P = 3$	$P = 4$
$\psi = 0^\circ$				
10	1.204×10^{-2}	4.998×10^{-4}	2.877×10^{-5}	1.692×10^{-6}
20	2.858×10^{-3}	5.542×10^{-5}	1.794×10^{-6}	5.345×10^{-8}
30	1.243×10^{-3}	1.601×10^{-5}	3.547×10^{-7}	7.060×10^{-9}
40	6.911×10^{-4}	6.693×10^{-6}	1.123×10^{-7}	1.678×10^{-9}
Order	2.062 ± 0.005	3.114 ± 0.024	4.001 ± 0.001	4.989 ± 0.002
$\psi = 30^\circ$				
10	1.255×10^{-2}	5.032×10^{-4}	2.878×10^{-5}	1.692×10^{-6}
20	2.896×10^{-3}	5.536×10^{-5}	1.793×10^{-6}	5.341×10^{-8}
30	1.246×10^{-3}	1.598×10^{-5}	3.544×10^{-7}	7.054×10^{-9}
40	6.894×10^{-4}	6.685×10^{-6}	1.122×10^{-7}	1.676×10^{-9}
Order	2.094 ± 0.009	3.120 ± 0.026	4.002 ± 0.001	4.989 ± 0.002

Table 10 Linear advection-diffusion results on regular grids using Witherden-Vincent and ϵ points

N	$P = 3$ (WV)	$P = 3$ (ϵ)	$P = 4$ (ϵ)
$\psi = 0^\circ$			
10	3.105×10^{-5}	1.525×10^{-4}	1.807×10^{-6}
20	1.909×10^{-6}	3.654×10^{-5}	6.546×10^{-8}
30	3.762×10^{-7}	1.606×10^{-5}	1.025×10^{-8}
40	1.190×10^{-7}	8.978×10^{-6}	2.887×10^{-9}
Order	4.014 ± 0.004	2.044 ± 0.007	4.655 ± 0.058
$\psi = 30^\circ$			
10	3.115×10^{-5}	1.560×10^{-4}	1.802×10^{-6}
20	1.910×10^{-6}	3.701×10^{-5}	6.483×10^{-8}
30	3.761×10^{-7}	1.620×10^{-5}	1.009×10^{-8}
40	1.189×10^{-7}	9.038×10^{-6}	2.829×10^{-9}
Order	4.017 ± 0.004	2.055 ± 0.008	4.668 ± 0.057

Table 11 Linear advection-diffusion results on irregular grids using Williams-Shunn points

N_{eles}	$P = 1$	$P = 2$	$P = 3$	$P = 4$
$\psi = 0^\circ$				
68	2.490×10^{-2}	1.995×10^{-3}	2.239×10^{-4}	1.921×10^{-5}
252	5.977×10^{-3}	2.559×10^{-4}	1.516×10^{-5}	6.562×10^{-7}
1042	1.499×10^{-3}	3.257×10^{-5}	8.476×10^{-7}	2.200×10^{-8}
2352	6.967×10^{-4}	9.272×10^{-6}	1.684×10^{-7}	2.643×10^{-9}
Order	2.014 ± 0.046	3.016 ± 0.034	4.062 ± 0.018	4.987 ± 0.057
$\psi = 30^\circ$				
68	2.298×10^{-2}	2.108×10^{-3}	1.953×10^{-4}	2.152×10^{-5}
252	5.897×10^{-3}	2.632×10^{-4}	1.368×10^{-5}	7.582×10^{-7}
1042	1.459×10^{-3}	3.122×10^{-5}	8.833×10^{-7}	2.064×10^{-8}
2352	6.642×10^{-4}	9.214×10^{-6}	1.660×10^{-7}	2.711×10^{-9}
Order	1.998 ± 0.022	3.061 ± 0.031	3.973 ± 0.032	5.072 ± 0.016

Table 12 Linear advection-diffusion results on irregular grids using Witherden-Vincent and ϵ points

N_{eles}	$P = 3$ (WV)	$P = 3$ (ϵ)	$P = 4$ (ϵ)
$\psi = 0^\circ$			
68	2.319×10^{-4}	3.221×10^{-4}	1.953×10^{-5}
252	1.565×10^{-5}	5.886×10^{-5}	6.868×10^{-7}
1042	8.711×10^{-7}	1.361×10^{-5}	2.589×10^{-8}
2352	1.729×10^{-7}	5.813×10^{-6}	3.609×10^{-9}
Order	4.068 ± 0.018	2.248 ± 0.091	4.826 ± 0.074
$\psi = 30^\circ$			
68	2.033×10^{-4}	3.048×10^{-4}	2.176×10^{-5}
252	1.415×10^{-5}	6.016×10^{-5}	7.834×10^{-7}
1042	9.079×10^{-7}	1.338×10^{-5}	2.471×10^{-8}
2352	1.704×10^{-7}	5.779×10^{-6}	3.829×10^{-9}
Order	3.981 ± 0.031	2.229 ± 0.067	4.887 ± 0.065

The 2D Navier-Stokes equations can be expressed in conservative form as

$$\frac{\partial W}{\partial t} + \frac{\partial}{\partial x}(\mathbf{F}_{adv} - \mathbf{F}_{dif}) + \frac{\partial}{\partial y}(\mathbf{G}_{adv} - \mathbf{G}_{dif}) = 0, \quad (68)$$

where

$$\mathbf{W} = \begin{Bmatrix} \rho \\ \rho u \\ \rho v \\ E \end{Bmatrix}, \quad \mathbf{F}_{adv} = \begin{Bmatrix} \rho u \\ \rho u^2 + p \\ \rho uv \\ u(E + p) \end{Bmatrix}, \quad \mathbf{G}_{adv} = \begin{Bmatrix} \rho v \\ \rho uv \\ \rho v^2 + p \\ v(E + p) \end{Bmatrix},$$

$$\mathbf{F}_{dif} = \mu \begin{Bmatrix} 0 \\ 2 \frac{\partial u}{\partial x} + \lambda \left(\frac{\partial u}{\partial x} + \frac{\partial v}{\partial y} \right) \\ \frac{\partial v}{\partial x} + \frac{\partial u}{\partial y} \\ u \left(2 \frac{\partial u}{\partial x} + \lambda \left(\frac{\partial u}{\partial x} + \frac{\partial v}{\partial y} \right) \right) + v \left(\frac{\partial v}{\partial x} + \frac{\partial u}{\partial y} \right) + \frac{C_p}{P_r} \frac{\partial T}{\partial x} \end{Bmatrix},$$

$$\mathbf{G}_{dif} = \mu \begin{Bmatrix} 0 \\ \frac{\partial v}{\partial x} + \frac{\partial u}{\partial y} \\ 2 \frac{\partial v}{\partial y} + \lambda \left(\frac{\partial u}{\partial x} + \frac{\partial v}{\partial y} \right) \\ u \left(\frac{\partial v}{\partial x} + \frac{\partial u}{\partial y} \right) + v \left(2 \frac{\partial v}{\partial y} + \lambda \left(\frac{\partial u}{\partial x} + \frac{\partial v}{\partial y} \right) + \frac{C_p}{Pr} \frac{\partial T}{\partial y} \right) \end{Bmatrix}.$$

In these equations, $\rho = \rho(\mathbf{x}, t)$ is the fluid density, $u = u(\mathbf{x}, t)$ and $v = v(\mathbf{x}, t)$ are the x - and y -velocity components, $E = E(\mathbf{x}, t)$ is the total energy, $p = p(\mathbf{x}, t)$ is the pressure, $T = T(\mathbf{x}, t)$ is the temperature, μ the dynamic viscosity, $\lambda = \frac{2}{3}$ is the bulk viscosity coefficient, C_p is the specific heat capacity, and $Pr = 0.72$ is the Prandtl number. The ideal gas law provides expressions for p and T as

$$p = (\gamma - 1) z \left(E - \frac{1}{2} \rho (u^2 + v^2) \right), \quad (69)$$

$$T = \frac{p}{\rho R}, \quad (70)$$

where $\gamma = 1.4$ is the ratio of specific heat and $R = 286.9 \frac{\text{J}}{\text{kg K}}$ is the specific gas constant for air.

5.2.1 2D Couette flow

The Couette flow problem considers the flow between two parallel plates of infinite extent along the x - z plane separated by a distance H in the y direction. The upper plate moves at a constant velocity u_w in the x direction while the lower plate remains stationary, and each plate is held at the same fixed temperature T_w . For a fixed viscosity μ , an analytic solution describing the flow takes the form

$$\rho_e(\bar{y}) = \frac{\gamma}{\gamma - 1} \frac{2p_0}{2C_p T_w + Pr u_w^2 \bar{y}(1 - \bar{y})}, \quad (71)$$

$$u_e = u_w \bar{y}, \quad (72)$$

$$v_e = 0, \quad (73)$$

$$E_e = p_0 \left[\frac{1}{\gamma - 1} + \frac{\frac{u_w^2}{2R} \bar{y}^2}{T_w + \frac{Pr u_w^2}{2C_p} \bar{y}(1 - \bar{y})} \right], \quad (74)$$

where $\bar{y} = \frac{y}{H}$ and p_0 is an initial constant pressure.

In this section, the Couette flow problem is solved on a finite rectangular domain $\Omega \in [0, 2] \times [0, 1]$ with periodic boundary conditions imposed on the left and right boundaries perpendicular to the plates. Isothermal boundary conditions are imposed on the lower and upper and upper boundaries

$$T(x, y = 0, t) = T_w, \quad (75)$$

$$T(x, y = 1, t) = T_w. \quad (76)$$

Additionally, the no-slip condition is imposed on the lower and upper boundaries,

$$u(x, y = 0, t) = 0, \quad (77)$$

$$v(x, y = 0, t) = 0, \quad (78)$$

$$u(x, y = 1, t) = u_w, \quad (79)$$

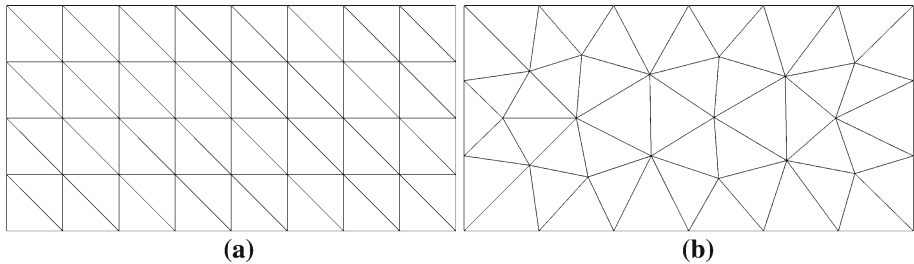


Fig. 7 Examples of meshes used for Couette flow test cases. **a** Regular Grid, $N = 8$. **b** Irregular Grid, $N_{\text{eles}} = 48$

$$v(x, y = 1, t) = 0, \quad (80)$$

which enforces zero velocity on the stationary plate, and a fixed x -velocity of u_w on the moving plate. For this test case, the wall temperature is set $T_w = 300\text{K}$ and the wall velocity is set $u_w = M\sqrt{\gamma RT_w}$ where the Mach number, $M = 0.2$. The remaining flow parameters were set to be consistent with a freestream Reynolds number $Re = 200$. The initial flow conditions are set to be constant with $\rho(\mathbf{x}, t = 0) = \langle \rho_e \rangle$, $u(\mathbf{x}, t = 0) = u_w$, $v(\mathbf{x}, t = 0) = 0$, and $p(\mathbf{x}, t = 0) = p_0$. Setting the initial density to $\langle \rho_e \rangle$, which denotes the average density computed over Ω , ensures that the amount of mass within the periodic domain is consistent with that of the analytic solution.

For this test case, the $L2$ error in the total energy is defined as

$$E_{L2}(t) = \sqrt{\int_{\Omega} (E(\mathbf{x}, t) - E_e(\mathbf{x}, t))^2 d\mathbf{x}}, \quad (81)$$

which as before is computed numerically using high strength element-wise quadrature. Time for this case is discretized using a standard RK4 scheme. The reported error is computed at $t = t_{ss}$ where t_{ss} is the time at which the energy solution reaches a steady-state. Using a similar metric as Witherden et al. [38], we compute the error every 1 time unit and define t_{ss} as the minimum time where the following criterion is met

$$\frac{E_{L2}(t_{ss})}{E_{L2}(t_{ss} + 1)} \leq 1.01, \quad (82)$$

This test case is carried out across several polynomial orders, P , on regular and irregular rectangular grids. The regular and irregular grids are similar to those used for the advection–diffusion problem and can be seen in Fig. 7. The order of accuracy computation is carried out in an identical manner to that in the previous section. For all orders, results using WS internal point locations are reported, along with additional results using the WV point locations reported for $P = 3$.

The order of accuracy results for this test case can be found in Tables 13 and 14. For most of the cases tested, an order of $P + 1$ is achieved, with a slight reduction in order reported for the case of $P = 2$ using WS points.

5.2.2 Viscous Flow Over a 2D Cylinder

To assess the performance of the DFR scheme in simulating unsteady viscous flow problems of engineering interest, we consider the solution to the unsteady Navier–Stokes equations

Table 13 Couette results on regular grids

N	$P = 1$	$P = 2$	$P = 3$ (WS)	$P = 3$ (WV)
4	1.332×10^{-4}	1.095×10^{-7}	2.409×10^{-8}	2.475×10^{-8}
6	5.896×10^{-5}	3.769×10^{-8}	4.682×10^{-9}	4.805×10^{-9}
8	3.310×10^{-5}	1.581×10^{-8}	1.495×10^{-9}	1.535×10^{-9}
10	2.134×10^{-5}	9.089×10^{-9}	6.814×10^{-10}	7.041×10^{-10}
Order	2.001 ± 0.006	2.745 ± 0.061	3.912 ± 0.074	3.907 ± 0.078

Table 14 Couette results on irregular grids

N_{eles}	$P = 1$	$P = 2$	$P = 3$ (WS)	$P = 3$ (WV)
8	3.110×10^{-4}	1.501×10^{-6}	1.086×10^{-7}	1.120×10^{-7}
22	1.073×10^{-4}	3.417×10^{-7}	1.667×10^{-8}	1.704×10^{-8}
48	4.237×10^{-5}	1.462×10^{-7}	2.292×10^{-9}	2.342×10^{-9}
86	3.187×10^{-5}	7.199×10^{-8}	1.268×10^{-9}	1.292×10^{-9}
Order	1.988 ± 0.171	2.536 ± 0.121	3.909 ± 0.331	3.918 ± 0.330

over a circular cylinder of infinite length at a Reynolds number $Re = 100$ at a fixed constant viscosity μ . At low Reynolds numbers, this problem can be modeled within a two-dimensional domain, perpendicular to the cylinder axis. This problem is simulated within a square domain $[-30, 70] \times [-50, 50]$ with a circular cylinder of diameter $D = 1$, centered at coordinate $(0, 0)$. The domain is partitioned into 4030 triangular elements with quadratic edges used to represent the cylinder wall. The resulting grid can be observed in Fig. 8. The outer boundaries of the domain are treated using Riemann-invariant characteristic boundary conditions [19] and an adiabatic, no-slip boundary condition is applied at the cylinder wall boundary. To minimize compressibility effects, the freestream velocity was set consistent with a Mach number $M = 0.1$.

For each case, the flow is marched forward in time using the low-storage RK45 [2R+] time integration scheme of Kennedy et al. [20] until a periodic laminar vortex shedding pattern is fully developed. At this point, the average and peak lift coefficients, C_L , and average and peak drag coefficients, C_D , are computed over ten shedding cycles, along with the Strouhal number, St . Plots of the time history of lift and drag coefficient over this period for the $P = 4$ case using WS points can be seen in Fig. 9 with an associated contour plot of vorticity in Fig. 10.

Results for the tested polynomial orders and internal point locations are listed in Table 15. Additionally, a comparison of the results achieved using $P = 4$ with WS internal points to those reported by others in previous studies can be found in Table 16. In comparing the results across polynomial order and point configuration, the lift, drag and Strouhal numbers are equivalent, indicating that the computational grid is adequately refined for this problem. This also provides further evidence that the scheme using WV points for $P = 3$ and ϵ points for $P = 4$ achieves similar numerical performance to the scheme using WS internal points. Comparison of the computed values with the reported results from several other studies show excellent agreement. This result provides support for the efficacy of the DFR scheme on triangles for simulating unsteady viscous flow phenomenon.

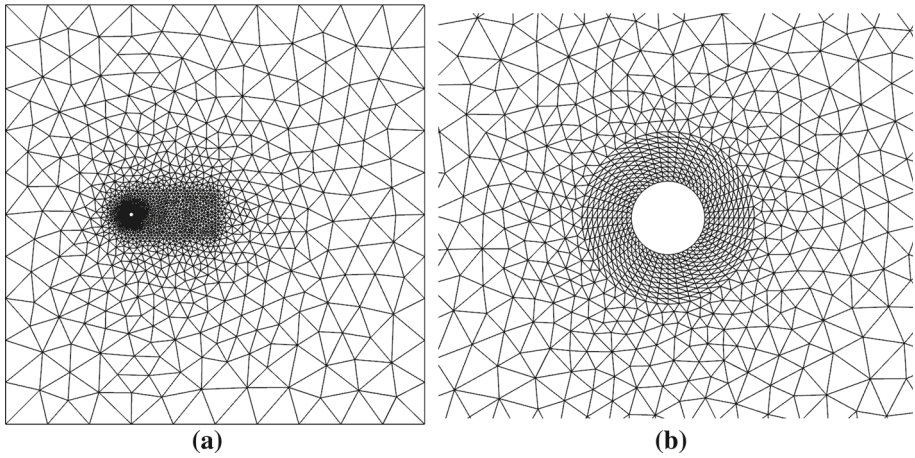


Fig. 8 Cylinder grid. **a** Full domain. **b** Closeup near cylinder

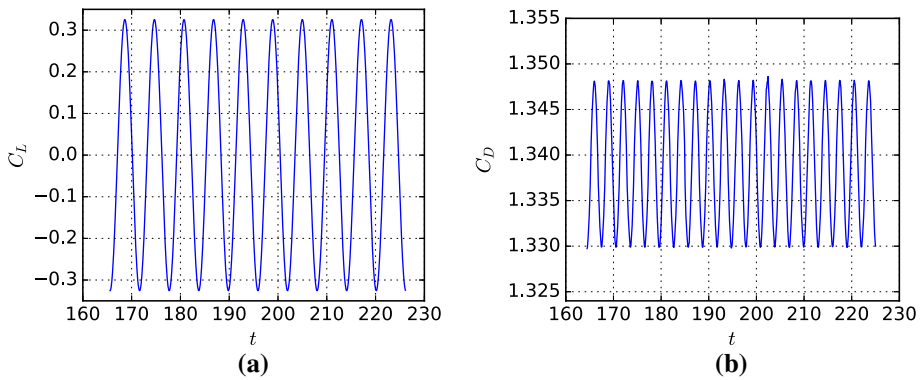


Fig. 9 Time history of lift and drag coefficients for cylinder at $Re = 100$, $P = 4$, Williams–Shunn points. **a** Lift. **b** Drag

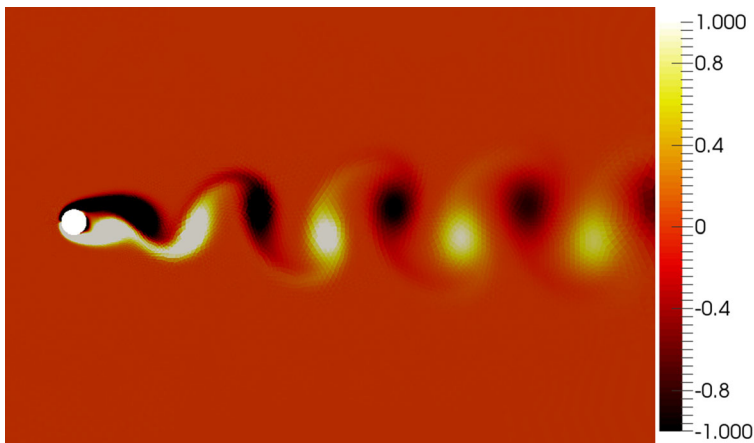


Fig. 10 Vorticity contours of cylinder at $Re = 100$, range scaled to $[-1, 1]$ for emphasis

Table 15 Cylinder results at $Re = 100$

P	Internal points	C_L	C_D	St
3	Williams–Shunn	± 0.326	1.339 ± 0.009	0.165
3	Witherden–Vincent	± 0.326	1.339 ± 0.009	0.165
4	Williams–Shunn	± 0.326	1.339 ± 0.009	0.165
4	ϵ	± 0.326	1.339 ± 0.009	0.165

Table 16 Cylinder results and comparison at $Re = 100$

Study	Method	C_L	C_D	St
Current	DFR ($P = 4$, WS points)	± 0.326	1.339 ± 0.009	0.165
Cox et al. [13]	Incompressible FR ($P = 3$)	± 0.325	1.339 ± 0.009	0.164
Chan et al. [6]	Spectral Difference ($P = 3$)	± 0.325	1.338 ± 0.009	0.164
Park et al. [26]	Fractional Step	± 0.332	1.33 ± 0.009	0.165
Sharman et al. [30]	SIMPLE	± 0.325	1.33 ± 0.009	0.164

6 Conclusion

This paper has extended the DFR approach to triangular elements for advection–diffusion problems. The resulting scheme benefits from a simple and straightforward implementation, relative to comparable ESFR formulations on triangles for the Navier–Stokes equations [37]. Although von Neumann analysis reveals the existence of weak linear instability for advection problems dependent on the placement of internal points for P greater than 2, the scheme is shown to produce stable and accurate solutions to various test problems, including those governed by the nonlinear Navier–Stokes equations. The identification of alternative internal point locations with varied numerical properties suggests the potential for future studies to uncover new internal point locations leading to schemes with favorable stability and numerical properties. Additionally, a new auxiliary variable computation method was introduced that utilizes the flux divergence computation to directly obtain untransformed gradient components. Beyond the DFR scheme presented in the current work, this procedure can be applied to the SD–RT scheme to extend its application to viscous problems. A natural extension of this formulation to tetrahedral elements should be possible, and is left to future studies.

Acknowledgements The authors would like to thank the Air Force Office of Scientific Research for their support via Grant FA9550-14-1-0186. The first author would like to acknowledge support from the Morgridge Family Stanford Graduate Fellowship.

Appendix

See the Table 17.

Table 17 ϵ point locations in barycentric coordinates, $\xi = (\xi_1, \xi_2, \xi_3)^T$

ξ_1	ξ_2	ξ_3
$P = 3$		
0.3333333333333333	0.3333333333333333	0.3333333333333333
0.055758983558155	0.055758983558155	0.88848203288369
0.88848203288369	0.055758983558155	0.055758983558155
0.055758983558155	0.88848203288369	0.055758983558155
0.290285227512689	0.070857385399496	0.6388573870878149
0.6388573870878149	0.290285227512689	0.070857385399496
0.290285227512689	0.6388573870878149	0.070857385399496
0.6388573870878149	0.070857385399496	0.290285227512689
0.070857385399496	0.290285227512689	0.6388573870878149
0.070857385399496	0.6388573870878149	0.290285227512689
$P = 4$		
0.034681580220044	0.034681580220044	0.9306368395599121
0.9306368395599121	0.034681580220044	0.034681580220044
0.034681580220044	0.9306368395599121	0.034681580220044
0.243071555674492	0.243071555674492	0.513856888651016
0.513856888651016	0.243071555674492	0.243071555674492
0.243071555674492	0.513856888651016	0.243071555674492
0.473372556704605	0.473372556704605	0.05325488659079003
0.05325488659079003	0.473372556704605	0.473372556704605
0.473372556704605	0.05325488659079003	0.473372556704605
0.200039998995093	0.047293668511439	0.752666332493468
0.752666332493468	0.200039998995093	0.047293668511439
0.200039998995093	0.752666332493468	0.047293668511439
0.752666332493468	0.047293668511439	0.200039998995093
0.047293668511439	0.200039998995093	0.752666332493468
0.047293668511439	0.752666332493468	0.200039998995093

References

1. Van den Abeele, K., Lacor, C., Wang, Z.: On the stability and accuracy of the spectral difference method. *J. Sci. Comput.* **37**(2), 162–188 (2008)
2. Allaneau, Y., Jameson, A.: Connections between the filtered discontinuous galerkin method and the flux reconstruction approach to high order discretizations. *Comput. Methods Appl. Mech. Eng.* **200**(49), 3628–3636 (2011)
3. Balan, A., May, G., Schöberl, J.: A stable high-order spectral difference method for hyperbolic conservation laws on triangular elements. *J. Comput. Phys.* **231**(5), 2359–2375 (2012)
4. Castonguay, P., Vincent, P.E., Jameson, A.: A new class of high-order energy stable flux reconstruction schemes for triangular elements. *J. Sci. Comput.* **51**(1), 224–256 (2012)
5. Castonguay, P., Williams, D., Vincent, P., Jameson, A.: Energy stable flux reconstruction schemes for advection-diffusion problems. *Comput. Methods Appl. Mech. Eng.* **267**, 400–417 (2013)
6. Chan, A.S., Dewey, P.A., Jameson, A., Liang, C., Smits, A.J.: Vortex suppression and drag reduction in the wake of counter-rotating cylinders. *J. Fluid Mech.* **679**, 343–382 (2011)
7. Cockburn, B., Hou, S., Shu, C.W.: The runge-kutta local projection discontinuous galerkin finite element method for conservation laws. iv. the multidimensional case. *Math. Comput.* **54**(190), 545–581 (1990)

8. Cockburn, B., Lin, S.Y., Shu, C.W.: Tvb runge-kutta local projection discontinuous galerkin finite element method for conservation laws iii: one-dimensional systems. *J. Comput. Phys.* **84**(1), 90–113 (1989)
9. Cockburn, B., Shu, C.W.: Tvb runge-kutta local projection discontinuous galerkin finite element method for conservation laws. ii. general framework. *Math. Comput.* **52**(186), 411–435 (1989)
10. Cockburn, B., Shu, C.W.: The runge-kutta local projection p^1 -discontinuous-galerkin finite element method for scalar conservation laws. *RAIRO-Modélisation mathématique et analyse numérique* **25**(3), 337–361 (1991)
11. Cockburn, B., Shu, C.W.: The local discontinuous galerkin method for time-dependent convection-diffusion systems. *SIAM J. Numer. Anal.* **35**(6), 2440–2463 (1998)
12. Cockburn, B., Shu, C.W.: The runge-kutta discontinuous galerkin method for conservation laws v: multidimensional systems. *J. Comput. Phys.* **141**(2), 199–224 (1998)
13. Cox, C., Liang, C., Plesniak, M.W.: A high-order solver for unsteady incompressible navier-stokes equations using the flux reconstruction method on unstructured grids with implicit dual time stepping. *J. Comput. Phys.* **314**, 414–435 (2016)
14. De Grazia, D., Mengaldo, G., Moxey, D., Vincent, P., Sherwin, S.: Connections between the discontinuous galerkin method and high-order flux reconstruction schemes. *Int. J. Numer. Methods Fluids* **75**(12), 860–877 (2014)
15. Hesthaven, J.S., Warburton, T.: *Nodal Discontinuous Galerkin Methods: algorithms, analysis, and applications*, **54**. Springer Verlag, New York (2008)
16. Huynh, H.: A flux reconstruction approach to high-order schemes including discontinuous Galerkin methods. *AIAA Pap.* **4079**, 2007 (2007)
17. Huynh, H.T.: A reconstruction approach to high-order schemes including discontinuous Galerkin for diffusion. In: 47th AIAA Aerospace Sciences Meeting including the New Horizons Forum and Aerospace Exposition, p. 403 (2009)
18. Jameson, A.: A proof of the stability of the spectral difference method for all orders of accuracy. *J. Sci. Comp.* **45**(1–3), 348–358 (2010)
19. Jameson, A., Baker, T.: Solution of the Euler equations for complex configurations. In: 6th Computational Fluid Dynamics Conference Danvers, p. 1929 (1983)
20. Kennedy, C.A., Carpenter, M.H., Lewis, R.M.: Low-storage, explicit runge-kutta schemes for the compressible navier-stokes equations. *Appl. Numer. Math.* **35**(3), 177–219 (2000)
21. Kopriva, D.A., Kolias, J.H.: A conservative staggered-grid Chebyshev multidomain method for compressible flows. *J. Comput. Phys.* **125**(1), 244–261 (1996)
22. Liu, Y., Vinokur, M., Wang, Z.: Spectral difference method for unstructured grids i: basic formulation. *J. Comput. Phys.* **216**(2), 780–801 (2006)
23. May, G., Schöberl, J.: Analysis of a Spectral Difference Scheme with Flux Interpolation on Raviart-Thomas Elements. Aachen Institute for Advanced Study in Computational Engineering Science, Aachen (2010)
24. Mengaldo, G., De Grazia, D., Moxey, D., Vincent, P.E., Sherwin, S.: Dealiasing techniques for high-order spectral element methods on regular and irregular grids. *J. Comput. Phys.* **299**, 56–81 (2015)
25. Mengaldo, G., Grazia, D., Vincent, P.E., Sherwin, S.J.: On the connections between discontinuous galerkin and flux reconstruction schemes: extension to curvilinear meshes. *J. Sci. Comput.* **67**(3), 1272–1292 (2016)
26. Park, J., Kwon, K., Choi, H.: Numerical solutions of flow past a circular cylinder at reynolds numbers up to 160. *KSME Int. J.* **12**(6), 1200–1205 (1998)
27. Raviart, P.A., Thomas, J.M.: A mixed finite element method for 2-nd order elliptic problems. In: Galligani, I., Magenes, E. (eds.) *Mathematical Aspects of Finite Element Methods*, pp. 292–315. Springer (1977)
28. Romero, J., Asthana, K., Jameson, A.: A simplified formulation of the flux reconstruction method. *J. Sci. Comput.* **67**(1), 351–374 (2016)
29. Rusanov, V.V.: The calculation of the interaction of non-stationary shock waves and obstacles. *USSR Comput. Math. Math. Phys.* **1**(2), 304–320 (1962)
30. Sharman, B., Lien, F.S., Davidson, L., Norberg, C.: Numerical predictions of low reynolds number flows over two tandem circular cylinders. *Int. J. Numer. Methods in Fluids* **47**(5), 423–447 (2005)
31. Vermeire, B., Witherden, F., Vincent, P.: On the utility of gpu accelerated high-order methods for unsteady flow simulations: a comparison with industry-standard tools. *J. Comput. Phys.* **334**, 497–521 (2017)
32. Vincent, P., Witherden, F., Vermeire, B., Park, J.S., Iyer, A.: Towards green aviation with python at petascale. In: *Proceedings of the International Conference for High Performance Computing, Networking, Storage and Analysis, SC '16*, pp. 1:1–1:11. IEEE Press, Piscataway (2016). <http://dl.acm.org/citation.cfm?id=3014904.3014906>
33. Vincent, P.E., Castonguay, P., Jameson, A.: Insights from von neumann analysis of high-order flux reconstruction schemes. *J. Comput. Phys.* **230**(22), 8134–8154 (2011)

34. Vincent, P.E., Castonguay, P., Jameson, A.: A new class of high-order energy stable flux reconstruction schemes. *J. Sci. Comput.* **47**(1), 50–72 (2011)
35. Williams, D., Jameson, A.: Energy stable flux reconstruction schemes for advection-diffusion problems on tetrahedra. *J. Sci. Comput.* **59**(3), 721–759 (2014)
36. Williams, D., Shunn, L., Jameson, A.: Symmetric quadrature rules for simplexes based on sphere close packed lattice arrangements. *J. Comput. Appl. Math.* **266**, 18–38 (2014)
37. Williams, D.M., Castonguay, P., Vincent, P.E., Jameson, A.: Energy stable flux reconstruction schemes for advection-diffusion problems on triangles. *J. Comput. Phys.* **250**, 53–76 (2013)
38. Witherden, F.D., Farrington, A.M., Vincent, P.E.: PyFR: an open source framework for solving advection-diffusion type problems on streaming architectures using the flux reconstruction approach. *Comput. Phys. Commun.* **185**(11), 3028–3040 (2014)
39. Witherden, F.D., Vincent, P.E.: An analysis of solution point coordinates for flux reconstruction schemes on triangular elements. *J. Sci. Comput.* **61**(2), 398–423 (2014)